High-density optical interconnects based on self-imaging in coupled waveguide arrays

J. Petrovic*, J. Kršić, A. Maluckov

Vinča Institute of Nuclear Sciences, National Institute of the Republic of Serbia, University of Belgrade, 12-14 Mike Petrovica Alasa, 11000 Belgrade, Serbia

J. J. P. Veerman

Fariborz Maseeh Department of Mathematics and Statistics, Portland State University, Portland, OR, USA

Abstract

Rapidly increasing demand for higher data bandwidths has motivated exploration of new communication channels based on spatially multiplexed in-fibre and on-chip coupled light guides. However, the conventionally used periodically arranged coupled waveguides display complicated light propagation patterns, ranging from quasiperiodic to nearly chaotic. Taking a different approach, we spectrally engineer interwaveguide coupling to instigate self-imaging of the input light state at the array output and thus enable construction of novel high-fidelity interconnects. Simple implementation via modulation of the interwaveguide separations makes these interconnects realizable in all fabrication platforms. Their competitive advantages are a negligible crosstalk-induced information loss, high density that exceeds the current standards by an order of magnitude, and compatibility with both classical and quantum information encoding schemes. Moreover, the wavelength-dependent self-imaging opens up new possibilities for wavelength and spatial division demultiplexing. The proposed analytical designs are supported by extensive numerical simulations of silicon-on-insulator, silicon nitride and silica glass waveguide arrays, and a sta-

*Corresponding author
Email address: jovanap@vin.bg.ac.rs (J. Petrovic)

tistical feasibility study.

Keywords: waveguide arrays, crosstalk, interconnects

1. Introduction

Optical transmission links and interconnects serve the modern industrial and consumer information markets and are seen as platform for future quantum information transfer [1]. Solutions for long-haul data transfer have pushed the signal multiplexing in time and wavelength domains to their technological limits [2, 3, 4]. The Big Data and Internet of Things put additional requirements on the short-range data transfer and routing to and from the network end-points. Finally, fibre-to-chip, intra-chip and on-chip interconnects built into the computer systems and smart phones are facing the input/output (I/O) bottleneck as the packaging density cannot sustain the demand for data bandwidth [5]. Therefore, the innovative solutions for light signal multiplexing and photonic device packaging are in high demand [6, 7].

In the last decade, spatial division multiplexing (SDM) has come to prominence as an underexploited highly-promising resource [8]. Development of optical fibres with multiple single- or multimode cores [9] and multimode waveguides on semiconductor chips [10], opened up new possibilities for mode and path division multiplexing [11]. Albeit compact and effective, the mode division multiplexing is limited by the inter-modal coupling that sets the maximum number of modes or propagation length along the fibre [12]. On the other hand, the first-generation path multiplexing through a bundle of single-core fibres has seen a wide-spread deployment in submarine cables. Due to the increased demand, considerable efforts are being invested in development of the second-generation links based on multicore fibres [13]. However, coupling between closely spaced cores, known as optical crosstalk, limits the link length or the number of cores. Thus the high-throughput transfer can be realized with fibres with large diameters but insufficient mechanical reliability [8]. In the same manner, crosstalk induces losses and limits the packaging density of waveguides in short and on-

chip interconnects [14, 15]. Hence, their usage relies on the crosstalk avoidance and source separation codes [16, 17, 18] or the strategies for waveguide isolation [19, 20, 21, 15], which significantly raises the system complexity and stands in opposition to the low cost per bit requirement. The most successful on-chip crosstalk reduction has been achieved by strong mode confinement in semiconductor interconnects with high refractive index (RI) contrast. Whereas this greatly reduces the footprint with respect to dielectric circuits [22, 23], the fundamental problem of the circuit size being limited by the crosstalk remains.

Consequently, disruptive SDM strategies that leverage on crosstalk have been considered [8]. It was suggested that the signal is encoded in eigenmodes of a coupled system, which propagate undisturbed over large distances [24]. However, complex I/O encoders and decoders are required to project the information to a corresponding eigenbasis. Another solution is provided by multiplexing of the orbital angular momentum (OAM) through multicore fibres with coupled cores [25]. Its prospective deployment depends on the development of sources and couplers for the high-order OAM light. Finally, the recently demonstrated transoceanic distance real-time transmission via a fibre with 4 coupled cores was aided by the time offset between signals in different cores to enable decorrelation at the receiving end [26].

Here, we take a new crosstalk-assisted approach to design high-density waveguide array (WGA) architectures that support high-fidelity on-chip, short-range and long-haul transmission. Our solution leverages on the linear coupling between waveguides to achieve periodic transmission and thus the full restoration of an input state at the output. The periodicity is realized by reverse spectral engineering of WGAs with commensurable eigenfrequencies, hereinafter commensurable waveguide arrays (CWGAs). The purely algebraic commensurability ansatz renders a generic design procedure for a variety of optical interconnects realizable with arbitrary waveguide RI profiles and waveguide densities.

The paper is structured as follows: In Section 1, we explain the idea on a model system composed of discrete nearest-neighbour coupled waveguides. In Section 3, we give examples of interconnects in low, medium and high RI con-

trast materials (silica glass (SiO_2), silicon nitride (SiN) and silicon-on-insulator (SOI)). We numerically estimate the gain in channel density and the classical and quantum link capacity scaling with the number of ports. In Section 4, we discuss the limitations of the model, present results of the feasibility check and estimate permissible fabrication tolerances. We summarize results and give a wider perspective in Section 5.

2. Methods

To demonstrate the commensurability principle and its application in interconnects, we model the waveguide coupling under two simplifying assumptions. The tight-binding approximation (TBA) allows for the representation of the fundamental mode of the j^{th} waveguide by a scalar complex wavefunction $\psi_j(z)$. The nearest-neighbour-coupling approximation yields the following tridiagonal model coupling matrix (Hamiltonian)

$$\mathbf{H} = \begin{pmatrix} \delta_1 & a_{1,2} & \cdots & & & \\ a_{2,1} & \delta_2 & & & & \\ & & \ddots & & & \\ & & & \delta_{M-1} & a_{M-1,M} \\ & & & a_{M,M-1} & \delta_M \end{pmatrix}, \tag{1}$$

where M is the number of waveguides in the array. The coupling matrix is composed of the real coupling coefficients $a_{j,k}$ and the relative phase detunings δ_j of waveguide modes. We assume that all waveguides are identical and hence the modes are phase matched with $\delta_j = 0$, $\forall j$. The propagation of a light state $\psi(z) = (\psi_1(z), \ldots, \psi_i(z), \ldots, \psi_M(z))^T$ along the array is calculated by solving the linear Schrödinger equation and results in

$$\psi(z) = \mathbf{T}\psi(0) = e^{-i\mathbf{H}z}\psi(0), \tag{2}$$

where $\mathbf{T}$ is the transfer matrix. $\mathbf{T}$ describes the functionality of the array and is calculated from the CWGA eigenspectrum by analytic expressions derived in [27].

The state transfer through a WGA interconnect is achieved by selection of the identity transfer matrix, $\mathbf{T}(kL) = \mathbf{I}$, whereby the interconnect length equals k multiples of the revival length L. A trivial analysis of the transfer matrix diagonalised in the form $(\mathbf{D}^{-1}\mathbf{T}\mathbf{D})_{j,k}(z = L) = e^{-i\Lambda_j L}\delta_{j,k}$, where Λ_j are the eigenfrequencies of the coupling matrix $\mathbf{H}$, shows that the equivalence condition is fulfilled for eigenfrequencies $\Lambda_j = n_j 2\pi/L$, where n_j are integers. This is nothing else but the eigenfrequency commensurability condition which ensures that the ratio of any two eigenfrequencies is a rational number.

CWGAs with equal coupling coefficients. In the case of uniform planar arrays, coupling matrix becomes a tridiagonal Toeplitz matrix with the eigenvalues $n_j = 2\cos\frac{m\pi}{M+1}$, $m = 1, 2, \ldots, M$. The arrays with $M < 4$ are periodic. Arrays with $M \geq 4$ have incommensurable eigenspectra and support quasi-periodic light propagation during which the input state is never restored, Fig. 1 f). As a consequence, a uniform WGA is suitable as an SDM interconnect only if the coupling between waveguides can be neglected along the whole array length, which requires large spacing between waveguides and thus limits the interconnect density. Interestingly, the analysis of a circular WGA geometry modelled by a Toeplitz matrix with $a_{M,1} = a_{1,M} \neq 0$, showed that the arrays with $M = 4$ and $M = 6$ waveguides can be stabilized by coupling the first to the end waveguide, while for other values of M also circular systems remain quasiperiodic [28].

CWGAs with unequal coupling coefficients. By allowing for different coupling strengths between the neighbouring waveguides the system coupling matrix becomes a type of Jacobi matrix and acquires new degrees of freedom. The eigenvalues of such a matrix are not readily available analytically [29], which significantly complicates the inverse engineering of CWGA. Particular solutions with Wannier-Stark eigenspectra are found in atoms, molecules or condensed matter systems with spin coupling [30] and their photonic simulators [31, 32]. Due to the unrestricted choice of integers n_j, our model allows for the general solutions beyond the arrays with equidistant eigenfrequencies [33, 34, 31], thus unlocking the potential for design of interconnects and other components, such as couplers and interferometers [35]. Here, we analyse applications of these

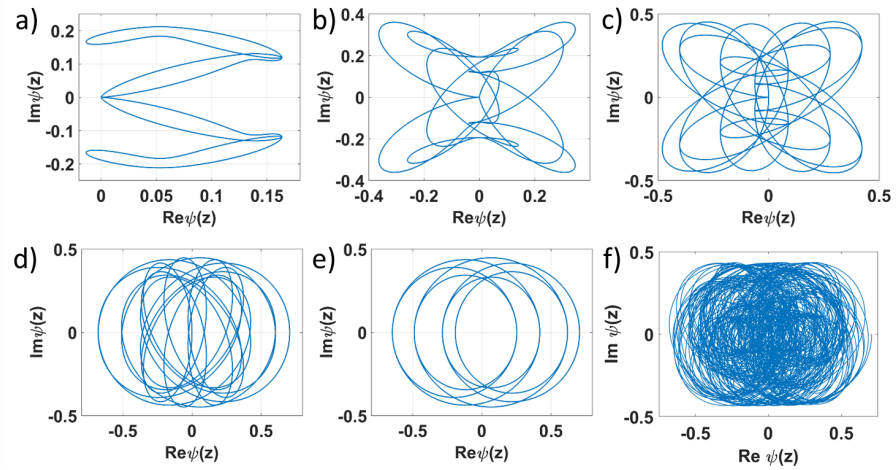

Figure 1: Light propagation through a mirror symmetric CWGA with 9 waveguides and the coupling coefficients $a_{1,2} = a_{8,9} = 1$, $a_{2,3} = a_{7,8} = 3.9965$, $a_{3,4} = a_{6,7} = 6.5000$, $a_{4,5} = a_{5,6} = 6.8516$. Shown are the phase plots of Im$\{\psi(z)\}$ vs. Re$\{\psi(z)\}$ over 100 revival lengths in different waveguides as follows: a) 1 and 9 (end waveguides) b) 2 and 8, c) 3 and 7, d) 4 and 6, and e) 5 (middle waveguide). The input state is $(0, 0, 0, 1, 1, 0, 0, 0, 0)$. f) The corresponding phase plot in waveguide 4 of a WGA with equal coupling coefficients.

solutions in interconnects as SDM systems.

The essential consequence of commensurable spectrum is the highly-ordered periodic light propagation [27, 36]. Its main signatures are the revivals of photon number and relative phases between waveguide modes. The photon number is revived with the maximum fidelity, $F = 1$, defined as $F(z) = (\sum_{j=1}^{M} |\psi_j(z)||\psi_j(0)|)^2$. The analogous result is obtained for the relative phases. Both types of revivals are evidenced in the periodic evolution of the mode wavefunction vectors in the complex plane, Fig. 1 a)-e). In a CWGA, all vectors repeat their paths within each revival length. In a non-commensurable WGA, at least one vector sweeps ever larger part of the complex plane and never repeats its path, Fig. 1 f). Importantly, the revivals are maintained upon any intervention on the input signal, thus allowing for application of different amplitude and phase modulation formats.

The proposed analytical model is ubiquitous and applies to any CWGA

Table 1: Properties of waveguides in different materials.

Material	Wavelength [nm]	shape	width [μm]	height [μm]	RI substrate	RI core	RI contrast [%]
SIO	1550	rectangular	0.4	0.3	1.444	3.673	42.3
SiN	800	rectangular	0.5	0.4	1.453	2.020	4.1
SiO_2	800	circular	3.5	3.5	1.453	1.460	0.5
SiO_2 fibre	1550	circular	8.2	8.2	1.445	1.450	0.5

embodiment in terms of RI profiles and nominal interwaveguide separations. The simplest way to realise the array experimentally is to control the coupling coefficients $a_{j,k}$ by adjusting the waveguide separations $d_{j,k}$ [37]. They are related by expression

$$a_{j,k} = Ae^{-\alpha d_{j,k}}, \tag{3}$$

where the coupling strength A and decrease rate α depend on the waveguide properties. Here, we support our claims derived from the analytical model by the full three-dimensional simulation of thus designed CWGAs. The waveguides finite width and height along the respective x and y axis was simulated by the finite difference model and the light propagation along z was simulated by the beam propagation method using the RSoft, Synopsis software.

3. Results

Based on the transmission length, optical interconnects can be broadly divided into the long-range interconnects with lengths spanning kilometers, short-range interconnects with lengths ranging from meters to centimeters, and on-chip interconnects of centimeter length and shorter. The minimum length of a CWGA interconnect is set by the revival length. Longer interconnects can be trivially realized by using multiple revival lengths. The shorter the revival length, the finer the control of the interconnect length.

Figure 2 compares revival lengths of CWGAs with different RI contrasts given in Table 1. RI contrast is here defined as $\frac{n_{core}^2 - n_{sub}^2}{2n_{core}^2}$, where n_{core} is the RI of the waveguide core and n_{sub} RI of the substrate. As there are infinitely many realizations of M-channel CWGA interconnects, all with different coupling

coefficients, we find that a waveguide pair ($M = 2$) described by a single coupling coefficient yields the fairest comparison. The revival length for the pair is given by $L = \pi/a$, where the coupling coefficient a exponentially decreases with the waveguide separation. Fine tuning of the waveguide separations allows for the continuous adjustment of the revival length over several orders of magnitude, from 10 μm to over 1 cm in SOI and SiN, from 1 mm to 10 cm on silica chip, and from 1 mm to 1 m in silica fibre.

The revival length further depends on the number of the constituent waveguides M. Here, we circumvent the problem of infinite number of CWGA realizations by providing an estimate for the well-known CWGAs with equidistant eigenfrequencies and spin-inspired coupling coefficients $a_{j,j+1} = \sqrt{j(M-j)}/2$. A simple calculation renders that the period scales as $\sqrt{M}$, which we confirmed numerically. For example, the ratio of the revival length of the interconnect with $M = 13$, Fig. 3 c), and the corresponding 2-waveguide interconnect is $3.5 \approx \sqrt{13/2}$.

To demonstrate applicability of the proposed analytical model to various fabrication platforms and substrates with different waveguide RI profiles and contrasts, we performed extensive simulations of waveguides with realistic parameters and show results in Fig. 3. Simulated are the interconnects on SOI, SiN and silica glass chips with the waveguide properties given in Table 1. We also show an interconnect composed of the cores of a typical single-mode step-index fibre, which is of relevance to multicore fibre transmission lines. The fibre and integrated interconnects in glass are represented by typical circular waveguide cross sections and low RI contrast achievable by fibre doping and direct laser writing. The semiconductor interconnects in SOI and SiN are composed of rectangular waveguides with high and medium index contrasts, respectively. They are simulated at separations by an order of magnitude smaller (few hundreds of nm) than in the conventional crosstalk-avoiding interconnects (few microns) [38].

The separations are not necessarily symmetric around the centre of the array. An asymmetric CWGA is fully described by $M-1$ parameters, whereas its eigenspectrum provides $M/2$ restrictions for even M and $(M-1)/2$ for odd M.

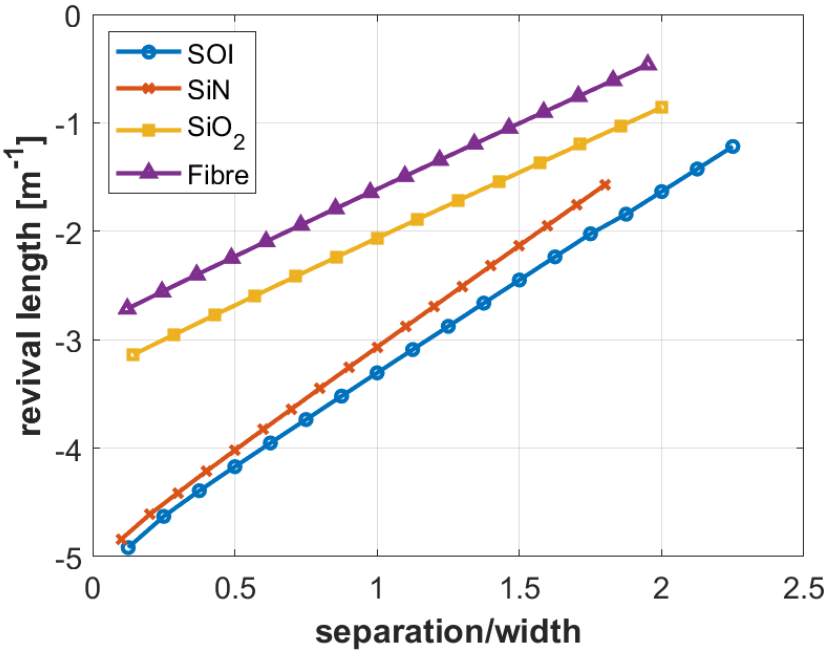

Figure 2: Scaling of the revival length with the interwaveguide separation for a pair of waveguides in different material platforms. A base-10 log scale is used for the Y axis. The waveguide properties are specified in Table 1.

The additional model parameters needed for array definition can be tuned to optimize the interconnect properties, such as bandwidth or I/O port geometry. On the other hand, a CWGA with the mirror symmetry is fully defined by its eigenfrequencies and no additional optimization of the array geometry is possible. As the small differences between interwaveguide separations and thus the waveguide asymmetry cannot be fully appreciated from the figure, we illustrate them by coupling symmetric states into asymmetric arrays in Fig. 3 (a) and (d). In the former, the power transfer occurs between equally excited waveguides and in the latter, the central excitation evolves into an asymmetric light pattern, both due to the inequality of coupling coefficients. Finally, to prove the capacity of an interconnect to faithfully transfer different input states, we excite the SiN interconnect with three arbitrarily chosen input states and obtain their

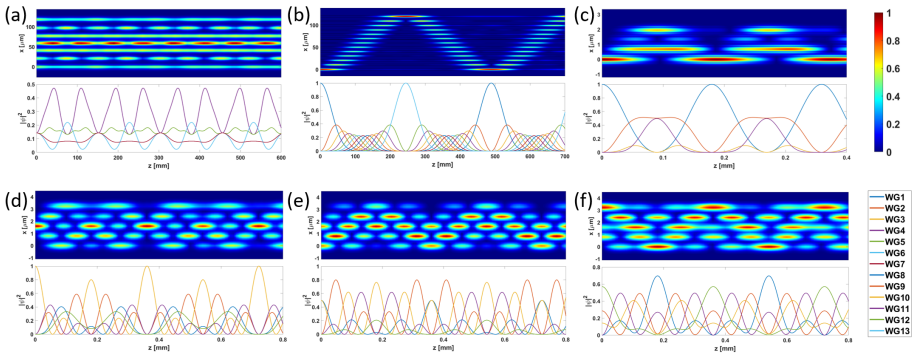

Figure 3: The light propagation through CWGA-based interconnects viewed from above. The light propagates from left to right. a) An array of 7 SMF-28e optical fibre cores at the minimum separation of 18 μm coupled with the coefficients $a_{1,2} = a_{6,7} = 1$, $a_{2,3} = a_{5,6} = 1.588$, $a_{3,4} = a_{4,5} = 3.111$ (color codes WG1-WG7), b) SiO_2 WGA with $M = 13$ waveguides at the minimum separation of 7μm and spin-inspired coupling coefficients $a_{j,j+1} = a_{j+1,j} = \sqrt{(M-j)j}/2$ (color codes WG1-WG13), c) SOI WGA with 4 waveguides with the minimum separation of 300 nm and coupling coefficients $a_{1,2} = 1$, $a_{2,3} = 1.213$, $a_{3,4} = 2.220$ (color codes WG1-WG4), d-f) SiN WGA with 5 waveguides at the minimum separation of 300 nm and coupling coefficients $a_{1,2} = 1$, $a_{2,3} = 0.989$, $a_{3,4} = 1.025$, $a_{4,5} = 0.667$ (color codes WG1-WG5) with different input states: d) (0,0,1,0,0), e) (1, 0, 1, 0, 0)/$\sqrt{2}$, f) (0, 1, 0.5, 0, 2)/$\sqrt{5.25}$. The properties of waveguides are specified in Table 1.

replicas at the output, Fig. 3 (d)-(f).

3.1. Classical link capacity

The capacity C of an SDM communication link can be estimated as $C \sim M \times B$, where M is the number of I/O ports, here simply the number of waveguides, and B is the data transfer rate per I/O port. The data transfer rate depends on multiplexing schemes and the signal-to-noise ratio [1]. In a typical application in which WDM is applied along SDM, B is proportional to the number of wavelength channels. The main bandwidth limiting factor in CWGA-based interconnects is the dependence of the interconnect length on wavelength. To quantify the extent of this limitation, we estimate the bandwidth of an SiN interconnect from Fig. 3(d) and give results in Fig. 4. To simulate the 'worst-case' scenario, only one waveguide is excited (please see section 4 for explanation

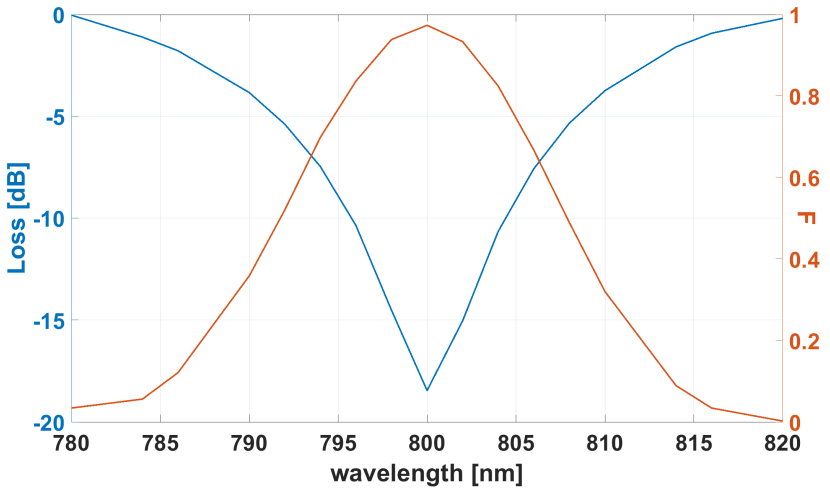

Figure 4: (a) Spectra of the average loss per channel and fidelity calculated for the SiN interconnect from Fig. 3(d).

of the 'worst case'). Assuming the maximum permissible loss of -12 dB and the minimum fidelity of 0.9, we obtain 2.8 THz bandwidth at 800 nm, a respectable bandwidth given that the primary design goal was SDM. As the revival length exponentially extends with increase in waveguide separation, dispersion effect is alleviated resulting in larger bandwidths for larger interconnects. For example, we simulated bandwidth of the same SiN interconnect with the separation increased to 700 nm and obtained 7 THz at 800 nm.

On the other hand, the revival-length dispersion can be used to our advantage. The fact that the optimal interconnect length is different for each wavelength channel can be used to construct a built-in wavelength demultiplexer, Fig. 5. The revival dispersion of the SiN interconnect with 300 nm waveguide separation is numerically estimated to be -2.4 μm/nm. Assuming the size of an add-drop filter of 20 μm [39], we obtain the impractical WDM channel spacing of 8.4 nm. However, exponential scaling of interconnect length with waveguide separation, makes the situation more favourable for larger interconnects. For example, increase in the waveguide separation to 700 nm increases

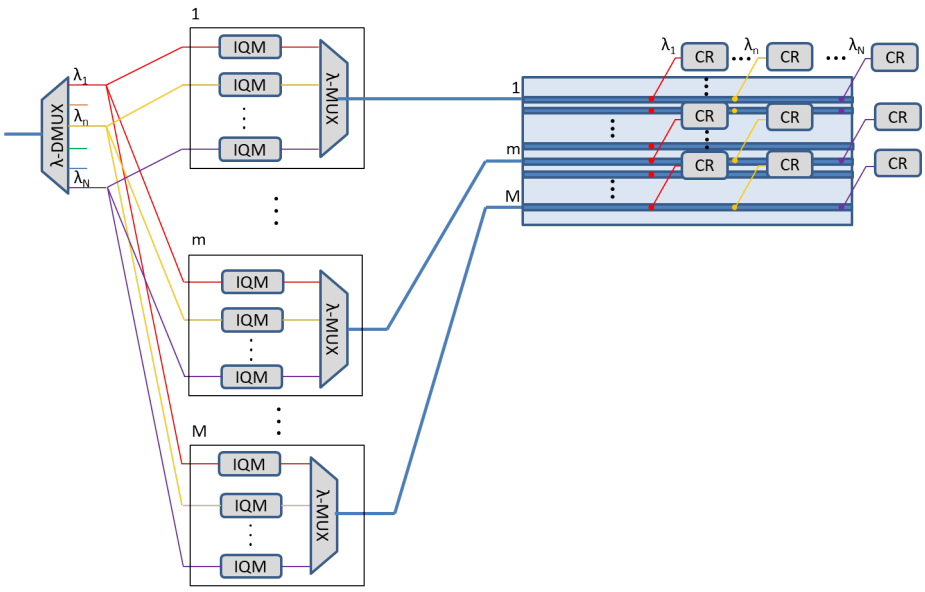

Figure 5: An example WDM-SDM system with a CWGA interconnect with built-in demultiplexer. MUX - multiplexer, IQM - IQ modulator , CR - coherent receiver.

the dispersion to -65.8μm/nm and thus brings the WDM channel spacing into the subnanometer regime. Moreover, due to the increase in interconnect length with the number of channels, demultiplexers with larger number of channels can support finer channel spacing. On a downside, the proposed demultiplexer requires out-of-plane filter design, which is yet to be demonstrated.

3.2. Quantum link capacity

To assess the suitability of CWGA interconnects for quantum information transfer, we evaluated the revivals of photon-coincidences. Namely, while self-imaging of a single photon corresponds to that of the coherent light, it is the transfer of multiple correlated photons that may yield the quantum advantage. We demonstrate the revivals of photon correlations on a path-entangled photon pair and its separable counterpart. The correlation of the former is represented by a coincidence matrix $\mathbf{\Gamma}^{ent}_{j,k}(z) = |\mathbf{T}_{j,p}(z)\mathbf{T}_{k,p}(z)+e^{-i\phi}\mathbf{T}_{j,q}(z)\mathbf{T}_{k,q}(z)|^2$, and of the latter by $\mathbf{\Gamma}^{sep}_{j,k}(z) = |\mathbf{T}_{j,p}(z)\mathbf{T}_{k,q}(z) + \mathbf{T}_{j,q}(z)\mathbf{T}_{k,p}(z)|^2$, where $\mathbf{T}(z)$

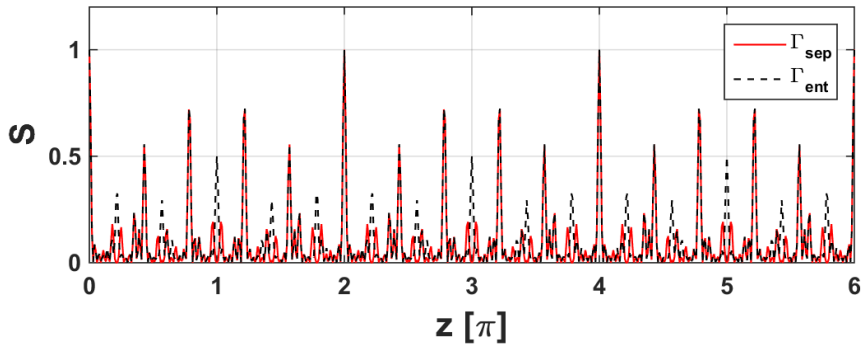

Figure 6: Similarity of the coincidence matrices of a separable (solid line) and correlated (dashed line) photon pairs inserted into waveguides 4 and 5 of the CWGA from Fig. 1.

is the CWGA transfer matrix [32]. The revivals are found as occurrences of the perfect overlap of a propagated coincidence matrix with its value at the input to the CWGA, whereby the overlap metric is the matrix similarity $S^{ent/sep} = \frac{\sqrt{(\sum_{j,k} \mathbf{\Gamma}_{j,k}^{ent/sep}(z=0)\mathbf{\Gamma}_{j,k}^{ent/sep}(z))^2}}{\sum_{j,k} \mathbf{\Gamma}_{j,k}^{ent/sep}(0) \sum_{j,k} \mathbf{\Gamma}_{j,k}^{ent/sep}(z)}$ [40]. Results show that both coincidence matrices experience periodic revivals, hence that the path entanglement is fully transferred, Fig. 6.

Quantum states can be encoded into different light properties, notably by the single-rail encoding into photon number and by d-rail encoding into different modes of the system (polarization, orbital angular momentum or waveguide modes) [41, 42, 43]. CWGA interconnects support all these encodings. Specifically, absence of bend-induced losses makes an M-waveguide CWGA suitable for transfer of M single-rail qubits encoded into M photons. The same array can carry $M/2$ dual-rail encoded qubits, each encoded into a single photon and 2 waveguides, or M/d d-iary qudits, each encoded into a single photon distributed over d waveguides. Alternatively, in the spirit of Cerf-Adami-Kwiat protocol [44], an M-waveguide CWGA can transmit $\log_2 M$ qubits or $\log_d M$ d-iary qudits encoded in a single photon distributed over the entire array.

4. Discussion

The main benefits of the crosstalk-friendly interconnects with respect to the conventional ones are the elimination of the crosstalk-induced information loss and increase in interconnect density. In the current model, the crosstalk-induced loss should not be present at all. This is, for example, evidenced in results of analytical calculations of power evolution through different interconnects in Fig. 3. In numerical simulations, the loss comes about due to the beyond-the-nearest-neighbour coupling and incomplete mode confinement. Namely, we integrate the intensity contained in the waveguide core only, while even its fundamental mode has evanescent field that extends beyond it. Figure 7(a) shows dependence of the average insertion loss per channel as a function of waveguide separation for the SiN interconnect with the waveguide separation of 300 nm. As the loss depends on the input state, we give results for two different input states from Fig. 3(d) and (f). The loss remains below -10 dB for all waveguide separations and both states. We note that the state that excites only one waveguide experiences higher loss than the state that excites more waveguides. Namely, for the single-port excitation, all losses from the non-zero output ports are registered as loss. For the multi-port excitation, the crosstalk between waveguides may lead to the power increase in non-zero output ports with respect to the input ports, which is not registered as loss. To complete the assessment in relevance to quantum computation, we evaluated fidelity as a function of the waveguide separation. The results shown in Fig. 7(b) confirm smaller robustness of the single-waveguide excitation and consistently high values of fidelity for multi-port excitation. Indeed, an order of magnitude reduction in the channel separation is possible without loss in performance.

The above numerical simulations were within the limits of validity of the nearest-neighbour coupling assumed in our model. However, the commensurability principle can be applied also to the arrays with significant long-range coupling by adding further side diagonals to the coupling matrix. In the asymptotic case of zero interwaveguide separation, arrayed waveguides merge into a

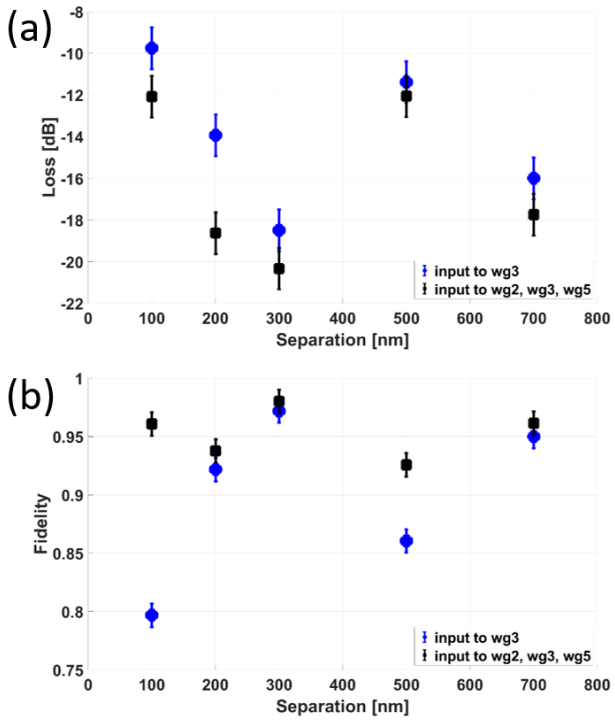

Figure 7: (a) Average loss per interconnect channel as a function of waveguide separation. (b) Fidelity as a function of waveguide separation. Simulated are SiN interconnects with properties from Table 1 with the input state (0, 0, 1, 0, 0) shown in blue and (0, 1, 0.5, 0, $2)/\sqrt{5.25}$ shown in black.

large bulk multimode waveguide and lose the advantage of singlemodedness. This advantage is important as it can provide automatic mode matching with the in- and out-coupling waveguides. Hence, the minimum interwaveguide separations are limited from below by the efficiency of light coupling in and out of CWGA. In the conventional circuits, such as multimode interference multiports, this is resolved by fanning the waveguides out, whereby the footprint of the coupling region dominates the interconnect. On the other hand, the efforts invested in investigation of WGA-based circuit components[35, 45, 46], along with the existing classical and quantum on-chip sources[47, 48] and detectors [49, 50], indicate the possibility of achieving all-WGA bend-free photonic

integrated circuits. Having the fabrication technology in place, a challenge before their realization are the demanding procedures for design of WGA-based components. The commensurability approach presented here is a stepping stone to this vision.

Finally, we report results of a comprehensive statistical feasibility check of CWGA fabrication. Dependence of the coupling coefficients and mode detunings (propagation constants) on the waveguide separations and RI profiles makes CWGA susceptible to the fabrication errors. We first used the analytical model of disordered coupling matrix in which the disorder is represented by the normal distribution of coupling coefficients and detunings around their design values with the relative standard deviations σ_{coupl} and σ_{det}, respectively. Thus obtained results are valid for any waveguide embodiment. They can be linked to a CWGA implementation of interest, by relating the relative standard deviations to those of the waveguide array parameters. In particular, from relation 2, we derive the relative deviation of the coupling coefficient $\sigma_{coupl} = -\alpha d \sigma_d$, where σ_d is the relative deviation of waveguide separations. Parameters α and d make this relation dependent on a concrete waveguide array embodiment. Similarly, the relative deviation of the detunings can be expressed as $\sigma_{det} = \sigma_{n_{eff}}$, where $\sigma_{n_{eff}}$ is the deviation of the effective-mode index and stems from the errors in waveguide refractive index and geometry.

We analyzed the disturbed system by calculating fidelity for 1000 randomly induced variations per each (σ_{coupl}, σ_{det}) point and finding the mean fidelity. Since the mean fidelity converged to dramatically different values for different input states and CWGA architectures, we ensured the 'worst-case' scenario by calculating the minimum mean fidelity across all input states. We performed the statistical analysis of both quenched (z-invariant) and non-quenched (random changes along z) disorder and found that these disorders lead to the same deterioration of fidelity.

Results for three different interconnect configurations given in Fig. 8 show that the variation in coupling coefficients consistently reduces the transfer fidelity by two orders of magnitude faster than the variation in detunings. In

particular, to reach fidelity $F > 0.95$, the coupling-coefficient tolerance should not exceed 0.35%, while the margin for detuning remains above 10%. The dominance of the coupling disorder, further amplified by the exponential dependence of coupling coefficient on waveguide separation, unambiguously defines the waveguide separation as the critical fabrication parameter. For example, using the expression given above, we estimate that an optimised SiN CWGA interconnect may tolerate 20 nm error in waveguide separations and 0.2 error in the waveguide RI, whereby we assumed that the waveguide dimensions were kept constant. Experimental demonstrations of the spin-simulating CWGAs show that the proposed interconnects can be accessed by the existing fabrication techniques, such as direct laser writing in glass [31, 32, 37] and lithography and reactive ion etching of semiconductors [40].

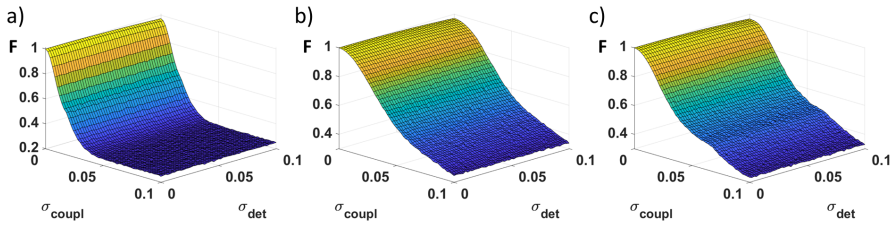

Figure 8: Fidelity in the presence of disorder in the coupling coefficients with the relative standard deviation σ_{coupl} and detunings with the relative standard deviation σ_{det}. Shown is the minimum fidelity across all possible initial states for the first revival in 5-waveguide CWGA interconnects with the coupling coefficients $a_{1,2} = a_{4,5} = 1$ and a) $a_{2,3} = a_{3,4} = 1.543$, b) $a_{2,3} = a_{3,4} = 0.624$ and c) $a_{2,3} = a_{3,4} = 2.739$.

5. Conclusion

We have addressed the challenge of constructing high density SDM links with interchannel crosstalk. The solution is based on CWGAs which support the full revival of any input state at the output. It is implemented by deriving the CWGA coupling matrix from a chosen commensurable eigenspectrum and ad-

justing the interwaveguide separations to attain the design coupling coefficients. The proposed approach enables construction of high-density interconnects with negligible crosstalk-induced losses and the length tunable over several orders of magnitude. They are accessible to the existing fabrication methods. Numerical simulations have shown a 10-fold increase in channel density. Relaxation of the tight-binding and nearest-neighbour approximations enables further increase up to the limits set by the specific output coupler size and efficiency. Even greater gains in footprint are expected in multiport WGA components without a preset length, such as couplers and interferometers. We see the proposed interconnects as a component of the future photonic integrated circuits composed solely of WGAs. The findings of this paper and the recent works of others show that such circuits are capable of handling both classical and quantum information, thus paving the way to the realization of ultimately small energy-efficient optical communication, computation and sensing hardware.

Acknowledgement

J. P., J.K. and A. M. acknowledge support from The Ministry of Science, Technological Development and Innovation of the Republic of Serbia, Grant No. 451-03-47/2023-01/ 200017. J. P. acknowledges useful discussions with U. Woggon and A. Achstein and M. Kleinert's generous help with defining SiN waveguide properties.

References

[1] W. Shi, Y. Tian, A. Gervais, Scaling capacity of fiber-optic transmission systems via silicon photonics, Nanophotonics 9 (16) (2020) 4629–4663. doi:doi:10.1515/nanoph-2020-0309.
URL https://doi.org/10.1515/nanoph-2020-0309

[2] G. Bosco, V. Curri, A. Carena, P. Poggiolini, F. Forghieri, On the performance of nyquist-wdm terabit superchannels based on pm-bpsk, pm-qpsk,

pm-8qam or pm-16qam subcarriers, Journal of Lightwave Technology 29 (1) (2011) 53–61. doi:10.1109/JLT.2010.2091254.

[3] A. Arnould, A. Ghazisaeidi, D. Le Gac, P. Brindel, M. Makhsiyan, K. Mekhazni, F. Blache, N. Fontaine, D. Neilson, R. Ryf, H. Chen, M. Achouche, J. Renaudier, 103 nm ultra-wideband hybrid raman/soa transmission over 3×100 km ssmf, Journal of Lightwave Technology 38 (2) (2020) 504–508. doi:10.1109/JLT.2019.2946590.

[4] M. Ionescu, D. Lavery, A. Edwards, E. Sillekens, D. Semrau, L. Galdino, R. I. Killey, W. Pelouch, S. Barnes, P. Bayvel, 74.38 tb/s transmission over 6300 km single mode fibre enabled by c+l amplification and geometrically shaped pdm-64qam, Journal of Lightwave Technology 38 (2) (2020) 531–537. doi:10.1109/JLT.2019.2954458.

[5] L. Alloatti, High-speed photonics for side-by-side integration with billion transistor circuits in unmodified cmos processes, Journal of Lightwave Technology 35 (6) (2017) 1168–1173. doi:10.1109/JLT.2017.2655420.

[6] J. Zhang, Z. Jia, Coherent passive optical networks for 100g/λ;-and-beyond fiber access: Recent progress and outlook, IEEE Network 36 (2) (2022) 116–123. doi:10.1109/MNET.005.2100604.

[7] D. A. B. Miller, Device requirements for optical interconnects to silicon chips, Proceedings of the IEEE 97 (7) (2009) 1166–1185. doi:10.1109/JPROC.2009.2014298.

[8] B. J. Puttnam, G. Rademacher, R. S. Luís, Space-division multiplexing for optical fiber communications, Optica 8 (9) (2021) 1186–1203. doi:10.1364/OPTICA.427631.
URL http://opg.optica.org/optica/abstract.cfm?URI=optica-8-9-1186

[9] Y. Yadin, M. Orenstein, Parallel optical interconnects over multimode waveguides using mutually coherent channels and direct detection, J. Light-

wave Technol. 25 (10) (2007) 3126–3131.
URL http://opg.optica.org/jlt/abstract.cfm?URI=jlt-25-10-3126

[10] H. Xu, D. Dai, Y. Shi, Silicon integrated nanophotonic devices for on-chip multi-mode interconnects, Applied Sciences 10 (18). doi:10.3390/app10186365.
URL https://www.mdpi.com/2076-3417/10/18/6365

[11] S. Murshid, B. Grossman, P. Narakorn, Spatial domain multiplexing: A new dimension in fiber optic multiplexing, Optics and Laser Technology 40 (8) (2008) 1030–1036. doi:https://doi.org/10.1016/j.optlastec.2008.03.001.
URL https://www.sciencedirect.com/science/article/pii/S003039920800042X

[12] S. Savović, A. Djordjevich, A. Simović, B. Drljača, Influence of mode coupling on three, four and five spatially multiplexed channels in multimode step-index plastic optical fibers, Optics and Laser Technology 106 (2018) 18–21. doi:https://doi.org/10.1016/j.optlastec.2018.03.015.
URL https://www.sciencedirect.com/science/article/pii/S0030399218302044

[13] C. Papapavlou, K. Paximadis, D. Uzunidis, I. Tomkos, Toward sdm-based submarine optical networks: A review of their evolution and upcoming trends, Telecom 3 (2) (2022) 234–280.
URL https://www.mdpi.com/2673-4001/3/2/15

[14] M. Haurylau, et al., On-chip optical interconnect roadmap: Challenges and critical directions, IEEE Journal of Selected Topics in Quantum Electronics 12 (6) (2006) 1699–1705.
URL https://doi.org/10.1109/JSTQE.2006.880615

[15] W. Song, et al., High-density waveguide superlattices with low crosstalk, Nature Communications 6 (1) (2015) 2027.
URL https://doi.org/10.1038/ncomms8027

[16] C. Qiao, R. Melhem, D. Chiarulli, S. Levitan, A time domain approach for avoiding crosstalk in optical blocking multistage interconnection networks, Journal of Lightwave Technology 12 (10) (1994) 1854–1862. doi:10.1109/50.337500.

[17] Y. Xiong, Y. Ye, H. Zhang, J. He, B. Wang, K. Yang, Deep learning and hierarchical graph-assisted crosstalk-aware fragmentation avoidance strategy in space division multiplexing elastic optical networks, Optics Express 28 (3) (2020) 2758–2777.
URL https://doi.org/10.1364/OE.381551

[18] C. Huang, D. Wang, W. Zhang, B. Wang, A. N. Tait, T. F. de Lima, B. J. Shastri, P. R. Prucnal, High-capacity space-division multiplexing communications with silicon photonic blind source separation, J. Lightwave Technol. 40 (6) (2022) 1617–1632.
URL http://opg.optica.org/jlt/abstract.cfm?URI=jlt-40-6-1617

[19] Y. Yang, Y. Guo, Y. e. a. Huang, Crosstalk reduction of integrated optical waveguides with nonuniform subwavelength silicon strips, Scientific Reports 10 (2020) 4491.
URL https://doi.org/10.1038/s41598-020-61149-1

[20] Y. Bian, Q. Ren, L. Kang, Y. Qin, P. L. Werner, D. H. Werner, Efficient cross-talk reduction of nanophotonic circuits enabled by fabrication friendly periodic silicon strip arrays, Scientific reports 7 (1) (2017) 1–9.
URL https://doi.org/10.1038/s41598-017-16096-9

[21] D. Kwong, et al., Corrugated waveguide-based optical phased array with crosstalk suppression, IEEE Photonics Technology Letters 26 (10) (2014) 991–994.
URL https://doi.org/10.1109/LPT.2014.2311454

[22] Y. Urino, et al., First demonstration of high density optical interconnects integrated with lasers, optical modulators, and photodetectors on single

silicon substrate, Optics Express 19 (26) (2011) B159–B165.
URL https://doi.org/10.1364/OE.19.00B159

[23] M. Smit, et al., An introduction to inp-based generic integration technology, Semiconductor Science and Technology 29 (8) (2014) 083001.
URL https://doi.org/10.1088/0268-1242/29/8/083001

[24] Y. Okawachi, O. Kuzucu, M. A. Foster, R. Salem, A. C. Turner-Foster, A. Biberman, N. Ophir, K. Bergman, M. Lipson, A. L. Gaeta, Characterization of nonlinear optical crosstalk in silicon nanowaveguides, IEEE Photonics Technology Letters 24 (3) (2011) 185–187.
URL https://doi.org/10.1109/LPT.2011.2177080

[25] L. Hadžievski, A. Maluckov, A. M. Rubenchik, S. Turitsyn, Stable optical vortices in nonlinear multicore fibers, Light: Science & Applications 4 (8) (2015) e314. doi:10.1038/lsa.2015.87.

[26] S. Beppu, M. Kikuta, K. Igarashi, H. Mukai, M. Shigihara, Y. Saito, D. Soma, H. Takahashi, N. Yoshikane, I. Morita, M. Suzuki, T. Tsuritani, Real-time transoceanic coupled 4-core fiber transmission, in: Optical Fiber Communication Conference (OFC) 2021, Optica Publishing Group, 2021, p. F3B.4. doi:10.1364/OFC.2021.F3B.4.
URL http://opg.optica.org/abstract.cfm?URI=OFC-2021-F3B.4

[27] J. Petrovic, J. Veerman, A new method for multi-bit and qudit transfer based on commensurate waveguide arrays, Annals of Physics 392 (2018) 128–141.
URL https://doi.org/10.1016/j.aop.2018.03.008

[28] A. Radosavljević, et al., Coherent light propagation through multicore optical fibers with linearly coupled cores, Journal of Optical Society of America B 32 (12) (2015) 2520–2527.
URL https://doi.org/10.1364/JOSAB.32.002520

[29] G. Meurant, A review on the inverse of symmetric tridiagonal and block tridiagonal matrices, SIAM Journal on Matrix Analysis and Applications 13 (3) (1992) 707–728. doi:10.1137/0613045.
URL https://doi.org/10.1137/0613045

[30] J. Petrovic, et al., A multi-state interferometer on an atom chip, New Journal of Physics 15 (4) (2013) 043002.
URL https://doi.org/10.1088/1367-2630/15/4/043002

[31] M. Bellec, G. M. Nikolopoulos, S. Tzortzakis, Faithful communication hamiltonian in photonic lattices, Optics Letters 37 (21) (2012) 4504–4506.
URL https://doi.org/10.1364/OL.37.004504

[32] M. Gräfe, A. Szameit, Integrated photonic quantum walks, Journal of Physics B: Atomic, Molecular and Optical Physics 53 (7) (2020) 073001. doi:10.1088/1361-6455/ab6cfc.
URL https://doi.org/10.1088%2F1361-6455%2Fab6cfc

[33] R. J. Chapman, et al., Experimental perfect state transfer of an entangled photonic qubit, Nature Communications 7 (2016) 11339.
URL https://doi.org/10.1038/ncomms11339

[34] R. Gordon, Harmonic oscillation in a spatially finite array waveguide, Opt. Lett. 29 (23) (2004) 2752–2754. doi:10.1364/OL.29.002752.
URL http://opg.optica.org/ol/abstract.cfm?URI=ol-29-23-2752

[35] J. Petrovic, Multiport waveguide couplers with periodic energy exchange, Optics letters 40 (2) (2015) 139–142.
URL ttps://doi.org/10.1364/OL.40.000139

[36] N. K. Efremidis, D. N. Christodoulides, Revivals in engineered waveguide arrays, Optics communications 246 (4-6) (2005) 345–356.
URL https://doi.org/10.1016/j.optcom.2004.11.009

[37] A. Szameit, S. Nolte, Discrete optics in femtosecond-laser-written photonic structures, Journal of Physics B: Atomic, Molecular and Optical Physics

43 (16) (2010) 163001.
URL https://doi.org/10.1088/0953-4075/43/16/163001

[38] V. Donzella, S. T. Fard, L. Chrostowski, Study of waveguide crosstalk in silicon photonics integrated circuits, in: P. Cheben, J. Schmid, C. Boudoux, L. R. Chen, A. Delâge, S. Janz, R. Kashyap, D. J. Lockwood, H.-P. Loock, Z. Mi (Eds.), Photonics North 2013, Vol. 8915, International Society for Optics and Photonics, SPIE, 2013, pp. 291 – 298. doi:10.1117/12.2042366.
URL https://doi.org/10.1117/12.2042366

[39] T. Barwicz, M. A. Popovic, P. T. Rakich, M. R. Watts, H. A. Haus, E. P. Ippen, H. I. Smith, Microring-resonator-based add-drop filters in sin: fabrication and analysis, Opt. Express 12 (7) (2004) 1437–1442. doi:10.1364/OPEX.12.001437.
URL https://opg.optica.org/oe/abstract.cfm?URI=oe-12-7-1437

[40] A. Peruzzo, et al., Quantum walks of correlated photons, Science 329 (5998) (2010) 1500–1503. doi:10.1126/science.1193515.
URL https://science.sciencemag.org/content/329/5998/1500

[41] Y. Wang, Z. Hu, B. C. Sanders, S. Kais, Qudits and high-dimensional quantum computing, Frontiers in Physics 8 (2020) 479. doi:10.3389/fphy.2020.589504.
URL https://www.frontiersin.org/article/10.3389/fphy.2020.589504

[42] D. Drahi, et al., Entangled resource for interfacing single- and dual-rail optical qubits, Quantum 5 (2021) 416. doi:10.22331/q-2021-03-23-416.
URL https://doi.org/10.22331/q-2021-03-23-416

[43] D. K. Burgarth, V. Giovannetti, Dual- and Multi-rail Encoding, Springer Berlin Heidelberg, Berlin, Heidelberg, 2014, pp. 87–122. doi:10.1007/978-3-642-39937-4_3.
URL https://doi.org/10.1007/978-3-642-39937-4_3

[44] N. J. Cerf, C. Adami, P. G. Kwiat, Optical simulation of quantum logic, Phys. Rev. A 57 (1998) R1477–R1480. doi:10.1103/PhysRevA.57.R1477.
URL https://link.aps.org/doi/10.1103/PhysRevA.57.R1477

[45] Y. Franz, M. Guasoni, Compact 1 × n power splitters with arbitrary power ratio for integrated multimode photonics, Journal of Optics 23 (9) (2021) 095802. doi:10.1088/2040-8986/ac1830.
URL https://doi.org/10.1088/2040-8986/ac1830

[46] Y. Lahini, G. R. Steinbrecher, A. D. Bookatz, D. Englund, Quantum logic using correlated one-dimensional quantum walks, npj Quantum Inf 4 (2018) 2. doi:10.1038/s41534-017-0050-2.
URL https://doi.org/10.1038/s41534-017-0050-2

[47] Z. Zhou, B. Yin, J. Michel, On-chip light sources for silicon photonics, Light: Science & Applications 4 (11) (2015) e358.
URL https://www.nature.com/articles/lsa2015131

[48] P. Senellart, G. Solomon, A. White, High-performance semiconductor quantum-dot single-photon sources, Nature nanotechnology 12 (11) (2017) 1026–1039.
URL https://www.nature.com/articles/nnano.2017.218

[49] W. Yang, J. Chen, Y. Zhang, Y. Zhang, J.-H. He, X. Fang, Silicon-compatible photodetectors: trends to monolithically integrate photosensors with chip technology, Advanced Functional Materials 29 (18) (2019) 1808182.
URL https://doi.org/10.1002/adfm.201808182

[50] W. H. Pernice, C. Schuck, O. Minaeva, M. Li, G. Goltsman, A. Sergienko, H. Tang, High-speed and high-efficiency travelling wave single-photon detectors embedded in nanophotonic circuits, Nature communications 3 (1) (2012) 1–10.
URL https://www.nature.com/articles/ncomms2307